Westfälische
Wilhelms-Universität
Münster

Bachelor thesis

Systematic study of jet widths in pp collisions at LHC

Submitted by

Paula Mors

27th December, 2021

First examiner
Apl. Prof. Dr. Christian Klein-Bösing

Second examiner
Prof. Dr. Anton Andronic

Westfälische Wilhelms-Universität Münster
Working Group Andronic/Klein-Bösing
Institute for Nuclear Physics

Declaration of Academic Integrity

I, *Paula Mors*, hereby confirm that this thesis on "Systematic study of jet widths in pp collisions at LHC" is solely my own work and that I have used no sources or aids other than the ones stated. All passages in my thesis for which other sources, including electronic media, have been used, be it direct quotes or content references, have been acknowledged as such and the sources cited.

Bad Sooden-Allendorf, 27th December 2021 ________________________________
Paula Mors

I agree to have my thesis checked in order to rule out potential similarities with other works and to have my thesis stored in a database for this purpose.

Bad Sooden-Allendorf, 27th December 2021 ________________________________
Paula Mors

Contents

1 Introduction

The ALICE experiment at the LHC detects particles resulting mostly from p p, p Pb and Pb Pb collisions. The particles occur in particle showers called jets. In general, there are gluon-induced jets which are broader and quark-antiquark jets. Since, jet widths also give information about the hadronization, these are interesting to investigate into. The influence of the strangeness on jet widths can get examinated by comparing jets with strange trigger particles like a $\mathrm{K^0_S}$ meson, Λ or $\overline{\Lambda}$ baryon with primary charged trigger particles. Another advantage of the selection of those samples is that it can be determined if the jet width is dependent on whether the produced particle is a meson or a baryon. Previous measurements like the one in [1], which investigated e^+e^- collisions with the OPAL detector, have shown that the relative production of Λ baryons is enhanced in gluon jets in comparison with quark jets while the the relative production of $\mathrm{K^0_S}$ mesons is comparable in both types of jets.

This thesis addresses the measurements of the jet widths resulting from pp collisions. In chapter 2, an overview over the theoretical background is given. It parts into a short introduction of elementary particles like quarks, composed systems and a general overview over jets. The data used in this paper originates from the ALICE experiment at the LHC. Therefore, chapter 3 provides an insight into the experimental set-up of ALICE.

After this, chapter 4 deals with actual data resulted from pp collisions at $\sqrt{s} = 13\,\mathrm{TeV}$. First, the selection criteria used beforehand and afterwards, the correlation function and its corrections are described. The correlation functions used in this thesis are h-h, $\mathrm{K^0_S}$-h and $(\Lambda + \overline{\Lambda})$-h whereas the trigger particle has a transverse momentum of $3\,\mathrm{GeV/c} < p_\mathrm{T}^\mathrm{trigg} < 20\,\mathrm{GeV/c}$. In section 4.4, the $\Delta\varphi$ and $\Delta\eta$ projections of the correlation function are presented, so that the single and double Gaussian fitting procedure of the projections is described in section 4.4.1 and section 4.4.2, respectively. These Gaussian fits are then used to calculate the FWHMs of the peaks in the correlation functions as described in section 4.5. The results are shown in section 4.6.

2 Theoretical Background

2.1 Quarks

In nuclear and particle physics, fundamental particles and compounds existing of them get addressed. Those can be categorized as fermions and bosons based on their half-integral or integral spin, respectively. A spin is the intrinsic angular momentum of a rudimentary particle. Elementary bosons, like the gluon, are the force carriers. Elementary fermions can be categorized into leptons, like an electron, or quarks. By definition fermions obey Fermi-Dirac statistics, whilst bosons obey Bose-Einstein statistics [2, 3].

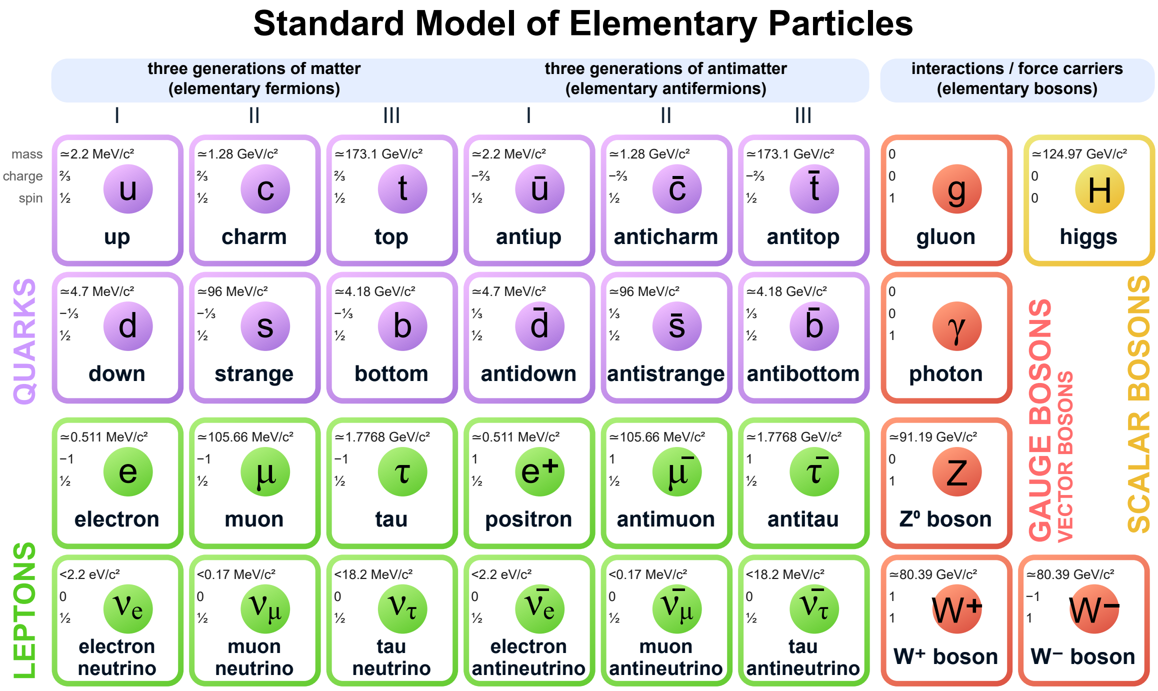

Figure 2.1: This diagram gives an overview of of the Standard Model where particles are classified as either quarks, bosons or leptons [4]. There is also shown the mass, charge and spin of each particle as well as for the leptons and quarks their generation and antiparticle. Especially relevant for this analysis are quarks and the gluon which will be discussed later.

There are six different types of quarks also called flavors, which are splitted in three quark-generations based on their mass as can be seen in Figure 2.1: up (u) & down (d), charm (c) & strange (s), top (t) & bottom (b) with an electric charge of $+\frac{2}{3}e$ and $-\frac{1}{3}e$, respectively. Here and in the following, e denotes the elementary charge. Besides the electric charge and the spin, all left-handed quarks and right-handed anti-quarks carry a weak isospin T with the third component $T_3 = +\frac{1}{2}$ for u, c and t and $T_3 = -\frac{1}{2}$ for d, s and b. Whilst the isospin I is a quantum number which describes the hadrons compound of first generation quarks, the weak isospin describes the electroweak interaction theory. Therefore, the quarks couple via the weak interaction as well. The equivalent charge regarding the strong interaction is the so called color. Each quark carries a color charge of red, green or blue, which is a theoretical concept and has nothing to do with the actual color. Besides quarks, there also exist their antiparticles with opposite charges, but the same mass called antiquarks. Therefore, anti-quarks can carry a color charge of either anti-red, anti-green or anti-blue [3].

Based on the confinement principle which will be discussed in detail later, it is not possible to isolate quarks. Thus, there exist only bound states of assembled quarks called hadrons, which may be separated in two types: baryons which are fermions and the bosonic mesons. The spin of the hadron constituents couple together to yield the hadron spin. Regarding the spin, the total quantum numbers get calculated based on quantum mechanical angular momentum addition. The constituent quark model assumes that hadrons are compounded only of valence quarks. Therefore, a baryon is composed of three constituent quarks while a meson exists of a quark-antiquark pair. For example, a proton as an uud state is a baryon and a pion π^+ as an $u\bar{d}$ state is a meson. The overall color charge of a bound state has to be white which means that either every color charge has to be represented or there is at least one pair of color with its anti-color [3].

2.1.1 Parton model

To be precise, hadrons do not consist just of two or three valence quarks, as stated in the constituent quark model, but also a variable amount of so called sea quarks and gluons. Whereas, a gluon is the exchange particle of the strong force, thus it is coupled to the color charge. This concept is called parton model. Next to hadron definition, valence quarks also determine its quantum numbers. The fundamental interaction Feynman diagrams are shown in Figure 2.2.

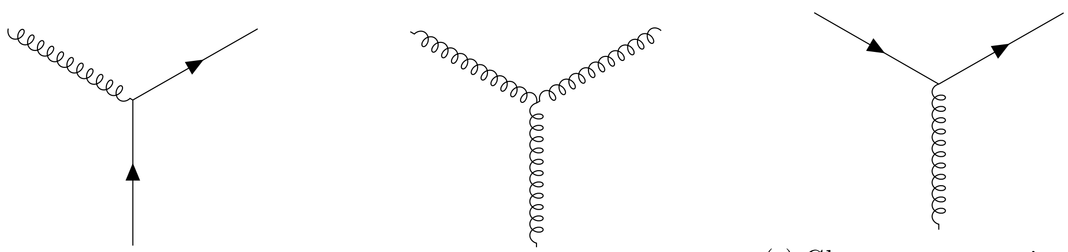

(a) Quark emits gluon

(b) Selfcoupling of gluons

(c) Gluon seperates into a quark-antiquark pair

Figure 2.2: Feynman diagrams of some fundamental quark-gluon interactions.

As one can see, a quark, like one of the valence quarks, may emit or absorb a gluon. There is also a selfcoupling of three or four gluons, only the former is visualized explicitly. Gluons can selfcouple because they have a color charge themselves. Furthermore, quark-antiquark-pairs can arise of gluons and afterwards annihilate back into gluons [3]. A schematic figure of the constituent quark model is shown in Figure 2.3. Because of the described interactions, there

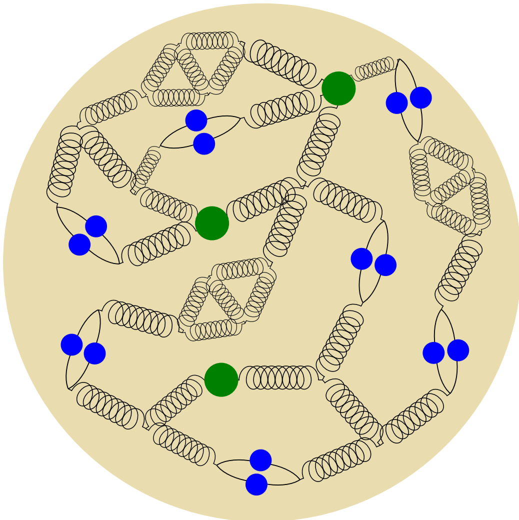

Figure 2.3: Schematic illustration of the parton model of a baryon, whereas valence quarks are green and sea quarks are blue.

is a continuous change of the internal color combinations and the amount of sea quarks. Nevertheless, the effective quantum numbers and the white color of the hadron stays the same, since those of the sea quarks cancel each other out. They still have an electric charge and are therefore visible in deep-inelastic scattering which means high energy lepton-hadron collisions [3].

2.1.2 Strange particles

K^0 mesons

The neutral kaon K^0 (valence quarks $d\bar{s}$) and its anti-particle $\overline{\mathrm{K}}^0$ decay into the same states. Therefore, they may convert into each other. As will be seen further on this leads to the $\mathcal{CP}$ violation, whereas $\mathcal{C}$ denotes the charge conjugating operator, so the particle-antiparticle exchange, and $\mathcal{P}$ denotes the parity operator, so the spatial reflection. Since the weak interaction only couples to left handed particles and right handed anti-particles, it violates the conservation of parity but the eigenvalue of the $\mathcal{CP}$ operator should be preserved. This could lead to the false assumption that this would be the case for the kaons K^0 and $\overline{\mathrm{K}}^0$, too [3]. By investigating their decay channels into two or three pions, one can see that these have different eigenvalues like

$$\mathcal{CP}\left|\pi^0\pi^0\right\rangle = +1\left|\pi^0\pi^0\right\rangle \qquad \mathcal{CP}\left|\pi^0\pi^0\pi^0\right\rangle = -1\left|\pi^0\pi^0\pi^0\right\rangle . \tag{2.1.1}$$

Moreover, the K^0 and $\overline{\mathrm{K}}^0$ mesons are no $\mathcal{CP}$ eigenstates

$$\mathcal{CP}\left|K^0\right\rangle = -1\left|\overline{\mathrm{K}}^0\right\rangle \qquad \mathcal{CP}\left|\overline{\mathrm{K}}^0\right\rangle = +1\left|\mathrm{K}^0\right\rangle. \tag{2.1.2}$$

In this case, the eigenvalue of the $\mathcal{CP}$ operator is not conserved which is called the $\mathcal{CP}$ violation. Since, one wants the weak interaction to preserve the $\mathcal{CP}$ symmetry, one defines mixed states like

$$\left|\mathrm{K}_1^0\right\rangle = \frac{1}{\sqrt{2}}\left(\left|\mathrm{K}^0\right\rangle - \left|\overline{\mathrm{K}}^0\right\rangle\right) \tag{2.1.3}$$

$$\left|\mathrm{K}_2^0\right\rangle = \frac{1}{\sqrt{2}}\left(\left|\mathrm{K}^0\right\rangle + \left|\overline{\mathrm{K}}^0\right\rangle\right) \tag{2.1.4}$$

which are now $\mathcal{CP}$ eigenstates with the eigenvalues $+1$ and -1, respectively. The result is that K_1^0 only decays into two and K_2^0 only into three pions. Because of the less probable appearance of three pions, one gets a kaon with a much longer lifetime compared to the other. The measured long-living K_L^0 and short-living K_S^0 do not correspond exactly to K_2^0 and K_1^0, because the former are mass eigenstates and the latter are the $\mathcal{CP}$ eigenstates. They are connected via

$$\left|\mathrm{K}_\mathrm{L}^0\right\rangle = \frac{1}{\sqrt{1+|\epsilon|^2}}\left(\epsilon\left|\mathrm{K}_1^0\right\rangle + \left|\mathrm{K}_2^0\right\rangle\right) \tag{2.1.5}$$

$$\left|\mathrm{K}_\mathrm{S}^0\right\rangle = \frac{1}{\sqrt{1+|\epsilon|^2}}\left(\left|\mathrm{K}_1^0\right\rangle + \epsilon\left|\mathrm{K}_2^0\right\rangle\right) \tag{2.1.6}$$

whereas the absolute value of the mixing parameter is about $|\epsilon| \approx 2.2 \times 10^{-3}$[3]. In the following, one looks at the K_S^0 mass eigenstate.

The most probable decay channel of K_S^0 is [5]:

$$\mathrm{K}_\mathrm{S}^0 \longrightarrow \pi^+ + \pi^-(69.2\,\%). \tag{2.1.7}$$

$\Lambda(\overline{\Lambda})$ hyperons

The valence quarks of a Λ hyperon are *uds*. A hyperon is a baryon with at least one strange, charm or bottom quark [6]. The u and d quarks of the Λ hyperon form together an isospin and a spin singlet state, and therefore the overall spin is carried only by the strange quark. If the u and d quark couple to an isospin and spin of one, the hyperon would be a Σ^0 hyperon. The mass difference between both hyperons is $80\,\mathrm{MeV/c^2}$ [3]. $\Lambda(\overline{\Lambda})$ hyperon's most probable decay channels with 63.9% are [5]:

$$\Lambda \longrightarrow p + \pi^- \tag{2.1.8}$$

$$\overline{\Lambda} \longrightarrow \overline{p} + \pi^+. \tag{2.1.9}$$

Λ, $\overline{\Lambda}$ and K_S^0 are also called V^0 particles. The V stands for the shape of their decay topology, which can be seen in Figure 2.4 and the 0 for their neutrality. Therefore, they cannot be tracked directly by a detector, but must be reconstructed from their daughter particles [7]. The reconstruction is illustrated as dotted lines in Figure 2.4 and based on the distance of

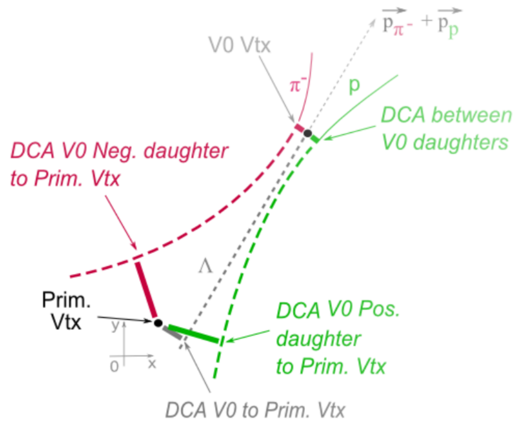

Figure 2.4: The Λ-hyperon decays V shaped into π^- and p [8].

closest approach (DCA). The Λ particle arises at the primary vertex (Prim. Vtx), where the pp collision takes place. At the secondary vertex the Λ particle decays into π^- and a proton. The distance between the primary and secondary vertex is the so called V^0 decay radius.

2.2 Jets and the quark-antiquark potential

Jets are basically tight packed showers of hadrons. They emerge when partons, after they are generated in a hard process, move in different directions and a gluon field arises. Because of the confinement, the quarks appear as quark-antiquark-pairs. To fully understand this phenomena, we will discuss the quark-antiquark potential first.

Comparing bound quark-antiquark with bound lepton-antilepton states like positronium, one finds similar energy levels. This implies a coulomb typed potential for short distances. However, due to the confinement principle and gluon self-interaction, the energy content of the gluon field does not decrease for great separations but rises linearly. Therefore, taking r as the distance between both quarks, we use the ansatz for the potential to be:

$$V(r) = \underbrace{-\frac{4\alpha_s(r)}{3r}}_{\substack{\text{Coulomb typed term}\\ \text{dominates for small r}}} + \underbrace{\kappa r}_{\substack{\text{linear term}\\ \text{dominates for large r}}} \tag{2.2.1}$$

in natural units which means that the speed of light c and the reduced Planck constant $\hbar$ are equal to one [2, 6].

This potential yields the correct asymptotic behaviour of $V(r \to 0) \propto \frac{1}{r}$ and $V(r \to \infty) \to \infty$. The factor of $\frac{4}{3}$ results of the fact that quarks occur in three different colors. In contrast to the implication of its name, the coupling constant of strong interaction α_s is not a constant, but depends on r. α_s is small for tiny r and therefore at small scales quarks may be seen as free which is called asymptotic freedom [3].

When separating quarks, the energy rises because of the linear term. In the Lund model, this gets visualized by a massless relativistic string, connecting a quark with an antiquark [9]. Therefore, κ is called string tension. In high energy processes, quarks get separated. Because of the string tension, the energy rises until it is high enough to create a new quark-antiquark pair. So in the picture of the Lund model, the string rips and the stored energy is used for the production of new quark-antiquark pairs. Together with the old partons, they assemble to new hadrons like it is shown in Figure 2.5. These hadrons are going to separate because they do not have the quark-antiquark potential but just the nuclear force between them. This process is called fragmentation [2].

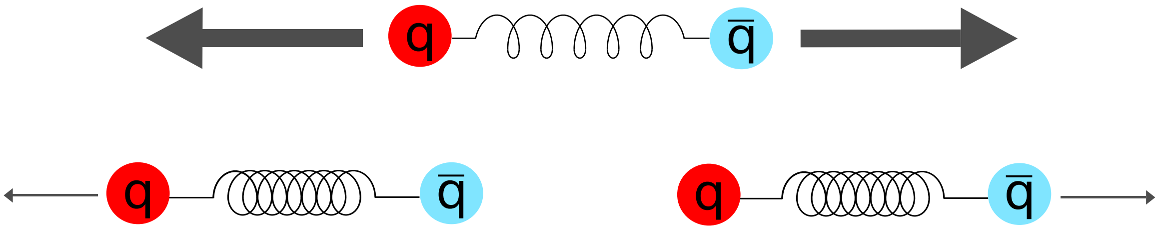

Figure 2.5: Graphical display of the confinement, whereas the colors do not describe the actual color charge.

Because of the conservation of momentum, these hadrons move in about the same direction as the initial quarks and the quark jets are formed. Neglecting transverse momentum effects in collision processes, the occurring jets point approximately towards opposite directions in the transverse plane. Figure 2.6 shows the orientation of the original quarks before and after fragmentation. Considering the transverse momentum effects p_T, the jets do not show a 180° angle but are slightly tilted which can be seen in the right part of Figure 2.6. These jets result in the so called near-side and away-side peak of the correlation function which will be discussed later.

Next to those explained 2-jet-events, in some cases, a 3-jet-event occurs. This is the case where the original quark emits a gluon which transforms in a quark-antiquark-pair forming third jet. This is a so called gluon jet [6].The largest difference between a gluon and a quark jet is that the multiplicity of a jet originating from a gluon is, if the asymptotic condition of $E_{\text{particle}} << E_{\text{jet}}$ is fulfilled, 9/4 of the quark jet [10]. Besides that, the angular width is larger and the fragmentation function is more soft. Therefore, gluon jets are broader than quark jets [11].

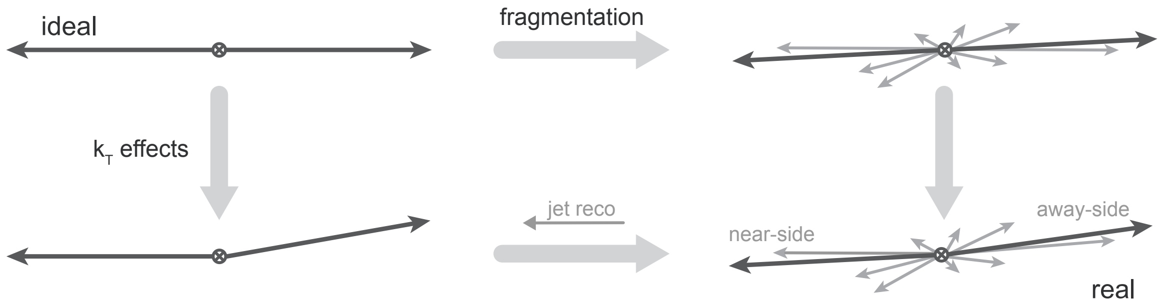

Figure 2.6: Formation of jets in the first line under ideal conditions and in the second line with considering transverse momentum ($\mathrm{p_T}$, here $\mathrm{k_T}$) effects [12].

Experiments have shown that baryons occur 2.5 times more in direct $\Upsilon(1S)$ decays than in continuum events via quark-antiquark fragmentation. For $\mathrm{K_S^0}$-mesons there is not such a trend. In gluon jets, the relative production of Λ baryons is around 40% higher than in quark jets [1].

2.2.1 Kinematics

The momentum of particles created in a collision can be separated into a longitudinal (p_L) and a transverse (p_T) momentum directing like the collision axis and in a perpendicular plane to it, respectively. In this thesis, we will use the z-axis as collision axis and define the lab system, as the center of mass system (CMS) of the two colliding hadrons. One must be aware that in the lab system, the interacting partons are not in their own CMS and therefore the propagator particle yields a longitudinal momentum. This results in the effect that even though two particles in the colliding hadrons CMS are emitted back to back, this is not the case in the lab system. Therefore, it is useful to describe particle collisions with Lorentz invariant variables.

Two of these variables are the transverse momentum $\vec{p}_T$ and the azimuthal angle φ around the beam, which are defined as [13]:

$$\vec{p}_T = (p_x, p_y) \tag{2.2.2}$$

$$\varphi = \arctan\left(\frac{p_x}{p_y}\right). \tag{2.2.3}$$

Another Lorentz invariant property is the difference of the rapidity which is always depending on two properties like the energy and the longitudinal momentum and therefore difficult to measure. An alternative is the geometric quantity pseudorapidity η which only depends on the polar angle θ between the momentum of the particle and the axis of the beam shown in Figure 2.7:

$$\eta = -\ln\left(\tan\left(\frac{\theta}{2}\right)\right). \tag{2.2.4}$$

This formula can be also written in terms of momentum:

$$\eta = \frac{1}{2} \ln \left(\frac{|p| + p_z}{|p| - p_z} \right). \tag{2.2.5}$$

Pseudorapidity is equal to rapidity for high momenta.

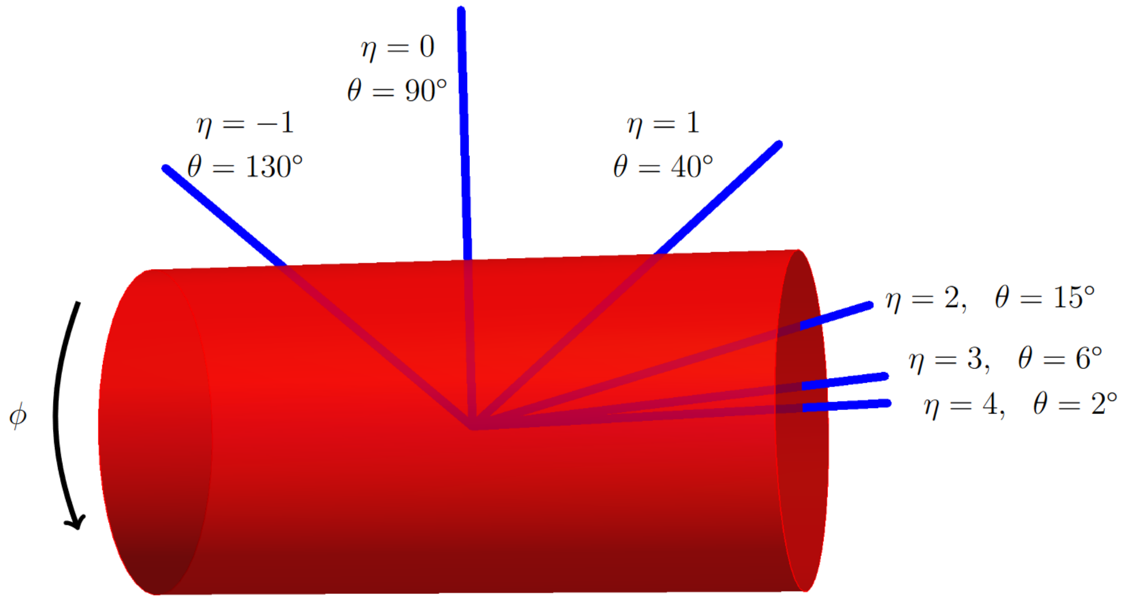

Figure 2.7: The pseudorapidity η, the polar angle θ and azimuthal angle φ (marked as ϕ in this figure), are graphically displayed. The red cylinder describes the full range of the azimuthal angle. Hypothetical, the beam axis lies in $\theta = 0$ direction [13].

The difference in pseudorapidity is Lorentz invariant for massless particles. Using these coordinates, a jet can be defined by a cone with the size $R = \sqrt{(\Delta\eta)^2 + (\Delta\varphi)^2}$ [13, 14].

3 Experimental set-up

The used data samples were collected by the ALICE detector. ALICE is an acronym for A Large Ion Collider Experiment. This 10 000 - tons detector is placed 56 m below ground at CERN, European Organization for Nuclear Research. The detector detects collisions from the synchrotron accelerator LHC (Large Hadron Collider) accelerated particles [15, 16]. An overview of the LHC layout is given in Figure 3.1, where one can see how the detectors are placed. There are also shown further pre-accelerators like the Super Proton Synchrotron (SPS).

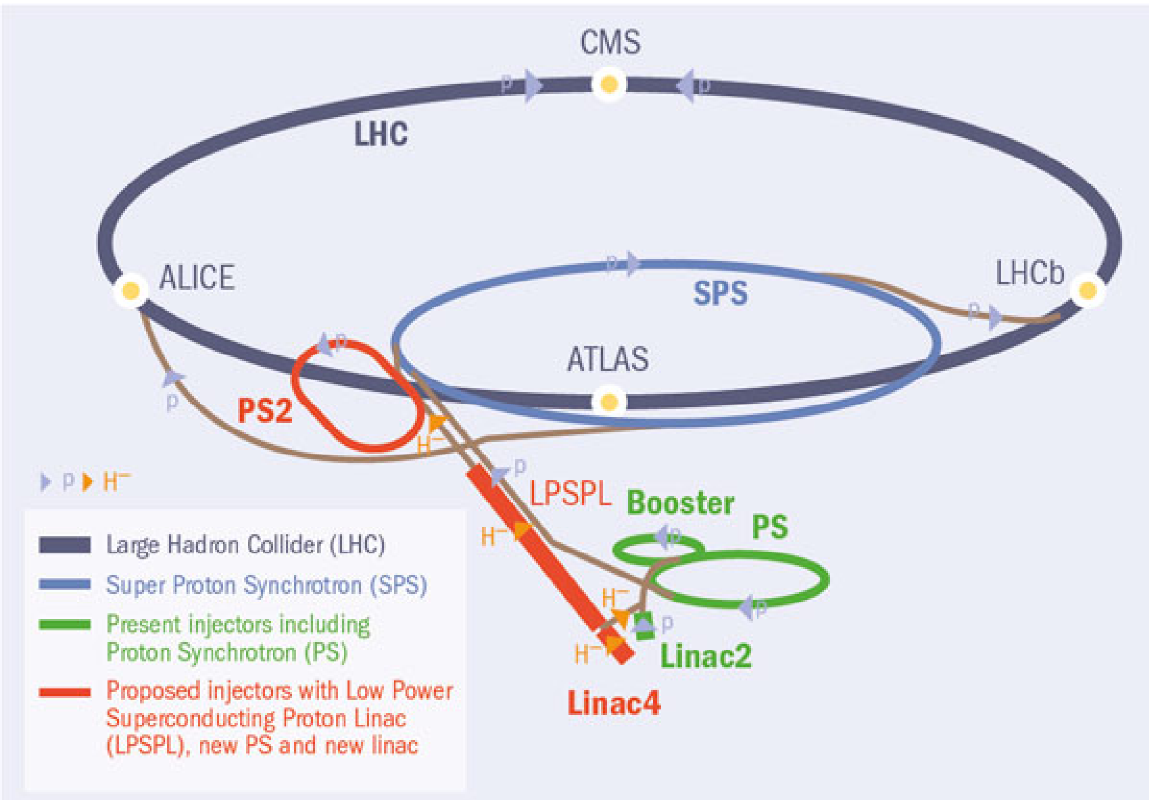

Figure 3.1: Shown is the schematic set up of the CERN acceleration complex [17].

3.1 LHC

The CERN accelerator complex consists of different machines which work with increasingly higher energies. The first machine expedites a beam of particles until it reaches a given energy then the beam gets injected into the next accelerator. This machine accelerates the beam more so that the energy is even higher. This goes so on until the LHC where the energy content of the colliding particles is the highest. In the LHC, two particle beams move in opposite directions in different pipes with a speed close to the speed of light. They are then forced to collide in one of the detectors, in this case the ALICE detector. The tubes, they travel in, are at ultrahigh vacuum. Electromagnets are cooled to a temperature of 1.9 K to be superconducting, encompass the accelerator ring by a strong magnetic field. Besides ALICE, there are six more experiments installed at the LHC called ATLAS, CMS, LHCf, LHCb, MoEDAL and TOTEM [18, 19]. Some of them can be seen in Figure 3.1.

3.2 ALICE experiment

The main purpose of the ALICE experiment is to investigate the quark-gluon plasma (QGP) and its physical properties [20]. The QGP is a state where gluons and quarks are not confined which probably took place a few microseconds after the big bang [15]. The ALICE detector set up of the LHC Run 2 is shown in Figure 3.2.

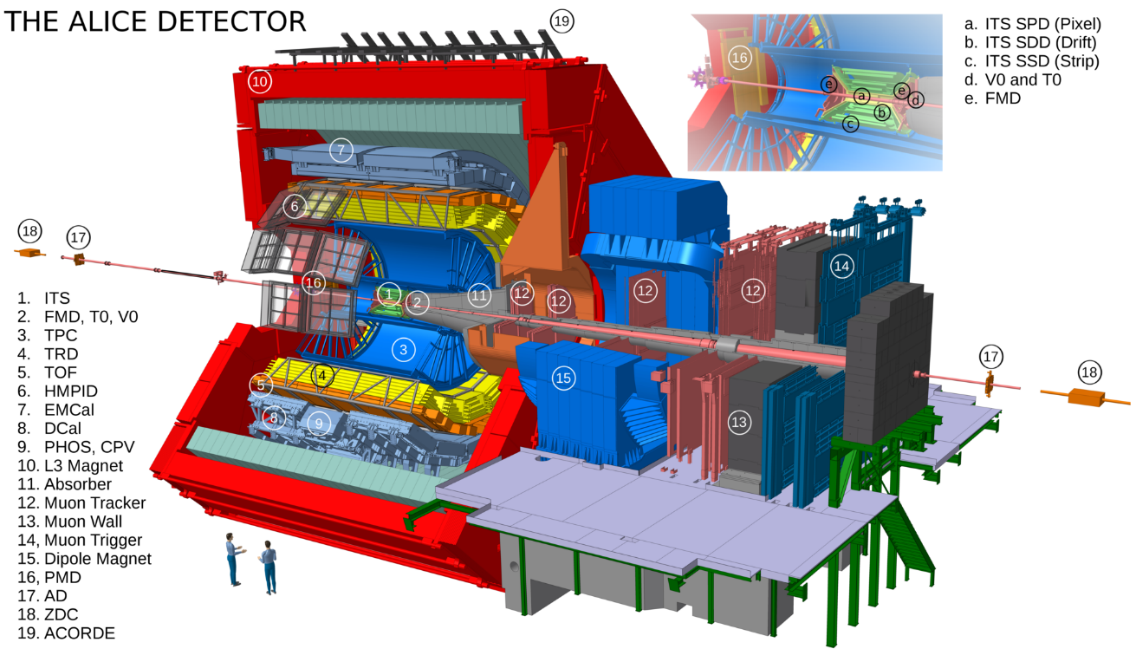

Figure 3.2: Set up of the ALICE detector at the LHC Run 2 [21].

3.2.1 Subdetectors

The ALICE detector exists mainly of a solenoid magnet which produces a magnetic field of 0.5 T and deflects the tracks of particles, which are charged, and different subdetectors. The subdetectors are set up as first a tracking system to seduce the path of the particles, secondly particle-identification detectors which as their name says determine the identity of the particles and lastly electromagnetic calorimeters which measure the energy of the electrons and photons [20]. In further, only subdetectors used for this particular analysis are described.

The Inner Tracking System (ITS) is a cylindrical detector which can differentiate if a particle originates in the collision or is a product of a fast decaying particle. The pseudorapidity range of reconstructed primary charged tracks is $|\eta|<0.9$. The ITS consists of six silicon tracking layers combining different technologies. For example two of them are Silicon Pixel Detectors (SPD)[7, 20].

Another subdetector besides the ITS is the Time Projection Chamber (TPC) which consists of a large drift volume. It is a cylinder which is filled with $90\,\mathrm{m}^3$ either of Ar/CO_2 (2016 and 2018) or $Ne/CO_2/N_2$ (2017). It is read out by multi-wire proportional chambers. The ITS and TPC are both placed in the central barrel and therefore called central barrel detectors. The information of both detectors together can be used to create a primary charged-track sample [7, 20].

The V0 detector exists actually out of two circular arrays with 32 scintillator counters respectively, called V0A and V0C. The detector is a plastic scintillator used as a part of ALICE's trigger system and to determine the event plane angle and centrality. The coincidental signal in both V0 arrays is used as MB trigger which can suppress recording of background processes as e.g. cosmic radiation. The forward scintillator arrays are covering pseudorapidity ranges of $-3.7 < \eta < -1.7$ and $2.8 < \eta < 5.1$ [20]. Further information about all subdetectors can be found in Ref. [20].

4 Data analysis

4.1 Selection criteria

Some selection criteria are used in the information gathering. There are triggers for the detectors needed to store information. Further selection criteria used can be found in [7, 22].

Event selection

For the event selection, a MB(minimum bias)-trigger is applied by the V0 detector. The trigger consists of two coincident signals in V0A and V0C [7]. Beam gas events[1] and pile-up events[2] get rejected by the V0 detector and the SPD, respectively [23]. Another requirement for a selected event is that the reconstructed primary collision vertex (PV) lays within the longitudinal interval $|z_{vtx}|<10\,\mathrm{cm}$ from the geometrical middle point of the detector, so that the detector performs uniformly [7].

Selection of V^0 and primary hadrons

The primary charged particle sample which is dominated by pions, gets reconstructed by the TPC and ITS in the range of $|\eta|<0.8$. Some selection criteria are needed to supersede the contamination from secondary particles. For example in the ITS the tracks have to hit the two most inner layers. The content of electrons in the selected sample of primary charged particles, is less than 1%[7].

The V^0 hadrons, K^0_S, Λ and $\overline{\Lambda}$, are neutral particles and therefore they must be tracked indirectly. The daughter tracks (as described in section 2.1.2) can be reconstructed and identified. The daughter tracks are combined and the V^0 candidates are selected on the invariant mass. Because of the specific energy loss, the daughter tracks can be identified by the TPC. The energy loss has to be essential within the range of $\pm 3\sigma$ from their expected mean value. The invariant mass of the identified daughter track pairs also has to be within the range of $\pm 3\sigma$ from the V^0 mass so that the daughter tracks are accepted as V0 candidates. The combinatorial background of the pairs of identified daughter tracks is reduced by applying a selection criteria which are based on the decay topology [7].

[1] A beam gas event describes the interaction of particles from the beam with gas atoms inside the beam-pipe.
[2] Pile-up events are additional pp collisions taking place in bunch-crossings.

4.2 Dihadron correlation function

A jet width can be determined via calculation of the widths of peaks in the correlation function. This is built by calculating the differences in pseudorapidity and azimuthal angle between trigger and associated particles. Trigger is a particle, which represents the direction of the leading hadron in a jet, associated particles are other particles within the same event, in this method primary charged hadrons [24]. In this data analysis, the trigger-particles K^0_S, Λ, $\overline{\Lambda}$ and primary charged hadrons (h) are selected in a high transverse-momentum interval between 3 and 20 GeV/c in pp collisions at $\sqrt{s} = 13\,\text{TeV}$. Another lower transverse momentum interval is used for the associated particles:

$$1\,\text{GeV/c} < p_T^{\text{assoc}} < p_T^{\text{trigg}}. \tag{4.2.1}$$

This results in three types of correlation functions: h-h, K^0_S-h, Λ-h and $\overline{\Lambda}$-h. The latest two are compatible at this collision energy and can therefore be combined as $(\Lambda + \overline{\Lambda})$-h for higher statistics. For those pairs of trigger and associated particles, the differences in the azimuthal angle and pseudorapidity are getting calculated and the two-dimensional correlation function can be constructed as [7, 22]:

$$\frac{d^2 N_{\text{pair}}}{d\Delta\varphi d\Delta\eta}(\Delta\varphi\Delta\eta) = \frac{1}{N_{\text{trigg}}}\frac{1}{\varepsilon_{\text{trigg}}}\frac{1}{\varepsilon_{\text{assoc}}}\frac{d^2 N^{\text{raw}}_{\text{pair}}}{d\Delta\varphi d\Delta\eta}\frac{1}{\varepsilon_{\text{pair}}}. \tag{4.2.2}$$

In this equation, N_{trigg} is the amount of trigger particles, $\frac{d^2 N^{\text{raw}}_{\text{pair}}}{d\Delta\varphi d\Delta\eta}$ is the uncorrected correlation function, and $\varepsilon_{\text{pair}}$, $\varepsilon_{\text{assoc}}$ and $\varepsilon_{\text{trigg}}$ are corrections which will be further discussed in section 4.2.1. Looking at Figure 4.1a one can see a peak at$(\Delta\varphi, \Delta\eta) = (0{,}0)$, called the

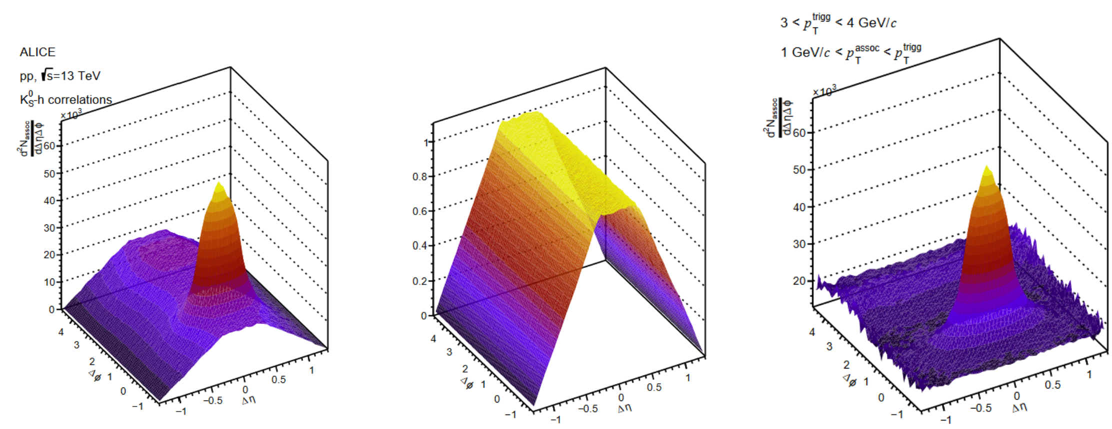

(a) raw correlation function (b) mixed-event correction (c) corrected correlation function

Figure 4.1: Graphically displayed is the mixed-event correction where on the left hand side the raw uncorrected same-event is shown. The plateaus in Figure 4.1a and Figure 4.1b are caused by non-equal selection in pseudorapidity of the associated and trigger particle [7].

near-side peak. It results mostly from pairs of particles, which are fragmented within the same jet. The yield of one peak after projecting on the $\Delta\varphi$ axis can be described as

$$Y_{\Delta\varphi} = \int_{\Delta\varphi_1}^{\Delta\varphi_2} \frac{dN}{d\Delta\varphi} d\Delta\varphi. \tag{4.2.3}$$

Because of the second jet described in section 2.2 which results from the conservation of momentum, another peak is present around π in $\Delta\varphi$ which can be seen in Figure 4.1c. This peak is smeared in the $\Delta\eta$ direction, resulting from an additional longitudinal boost of the particles. This can be explained by the varied center-of-mass frame of the partons in the pp collision. Therefore, it can happen that this away-side jet is not completely within the detector acceptance [7, 22]. The widths of these peaks can be assigned as the jet widths and will be estimated as FWHM.

4.2.1 Corrections

The corrections are used to correct for detection unefficiencies, definite detector acceptance and misidentified V^0.

Mixed event method ($\varepsilon_{\mathrm{pair}}$)

The detector acceptance is limited and therefore corrections have to be made to compensate the geometric correlation shaped of a triangle seen in the raw correlation function in Figure 4.1a. One opportunity to do so is to use the mixed event method marked as $\varepsilon_{\mathrm{pair}}$ in Equation 4.2.2. Trigger particles of one event are getting correlated with associated particles from other events so no physical correlation can occur. Therefore, the corrected correlation function can be calculated as follows:

$$\frac{d^2 N_{\mathrm{pair}}}{d\Delta\varphi, d\Delta\eta}(\Delta\varphi, \Delta\eta) = \sum_i \frac{S_i(\Delta\varphi, \Delta\eta)}{\frac{1}{\alpha_i} M_i(\Delta\varphi, \Delta\eta)} \tag{4.2.4}$$

whereas i is the primary vertex position, $S_i(\Delta\varphi, \Delta\eta)$ the correlation function of same events and $M_i(\Delta\varphi, \Delta\eta)$ the correlation function of mixed events. This mixed correlation function is shown in Figure 4.1b. The background shape does not get corrected very well with this method for h-h correlations. At the away side peak, small wings appear and therefore another correction must be performed, called wing-correction, to flatten this distribution in $\Delta\eta$ direction [22].

Single-particle efficiency correction ($\varepsilon_{\mathrm{assoc}}$ and $\varepsilon_{\mathrm{trigg}}$)

The efficiency of particle reconstruction is not 100 %, but it can be corrected by using simulation informations from the Monte Carlo (MC) event generators. Another criteria for both associated and trigger particles is that the reconstructed candidates need to be primary. The single-particle efficiency is defined as:

$$\varepsilon_{\text{assoc/trigger}} = \frac{N^{\text{rec}}_{\text{primary assoc/trigger}}}{N^{\text{gen}}_{\text{primary assoc/trigger}}}. \tag{4.2.5}$$

Here, N indicates the number of reconstructed (rec) and generated (gen) primary hadrons, respectively and the pseudorapidity acceptance for primary tracks was limited to $|\eta| < 0.8$. This correction was not only done for the primary charged hadrons but also for the V^0 particles [22].

Further corrections

The selection criteria do not differentiate between primary and for example secondary particle tracks, just if they are charged or not. Therefore, a correction to distinguish between them has to be made which is called secondary contamination correction. One further correction is called correction for the contribution of misidentified V^0. This must be performed because some V^0 candidates are satisfying the selection criteria, but are misidentified and therefore no real V^0. To correct that in the correlation function, a second correlation function needs to be computed. In this function, the invariant mass spectrum is used to pick trigger particles from sideband regions. Further corrections can be seen in Reference [22].

4.3 ROOT

The software used in this analysis is called ROOT [25]. It is a framework for data processing and got designed at CERN to visualise large amounts of data. ROOT is written in C++, but it can be linked to other programming languages like Python, thanks to its converter for coding languages. The software offers varieties of presenting the data for example in histograms or scatter plots. It supports different histogram classes, which are categorised by their set of possible bin values. The histogram types, we use are called TH1D and TH2D, where as the number shows the amount of dimensions. TH1D and TH2D contain one double per bin with a maximum precision of 14 digits [26].

4.4 Projections

One of the resulting correlation function is shown in Figure 4.2. The larger peak is the near-side peak and the smaller one the away-side peak. To investigate those peaks, we once look at the TH1D $\Delta\varphi$ projection for $|\Delta\eta| < 1$ (Figure 4.3a) and for $\Delta\eta$ projection in range $-\frac{\pi}{2} < \Delta\varphi < \frac{\pi}{2}$ (Figure 4.3b), where all bins are added up. In this analysis, three correlation functions, h-h, K^0_S-h, $(\Lambda + \overline{\Lambda})$-h, get examined. Each dataset includes further eight correlation functions calculated in the following p_T^{trigg} intervals: 3-4 GeV/c, 4-5 GeV/c, 5-6 GeV/c, 6-7 GeV/c, 7-9 GeV/c, 9-11 GeV/c, 11-15 GeV/c, 15-20 GeV/c. For each of the in total 24 correlation functions both, $\Delta\varphi$ and $\Delta\eta$, projections are created to investigate the

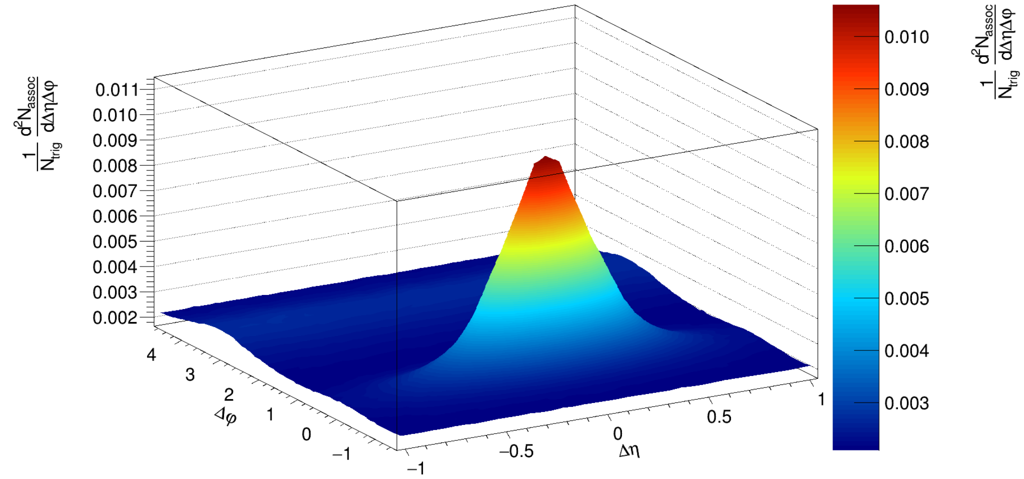

Figure 4.2: Correlation function of h-h at $p_{\mathrm{T}}^{\mathrm{trigg}} = 3\text{-}4\,\mathrm{GeV/c}$, whereas $\Delta\varphi$ and $\Delta\eta$ are given in radiant.

jet width via determining the full width at half maximum (FWHM).

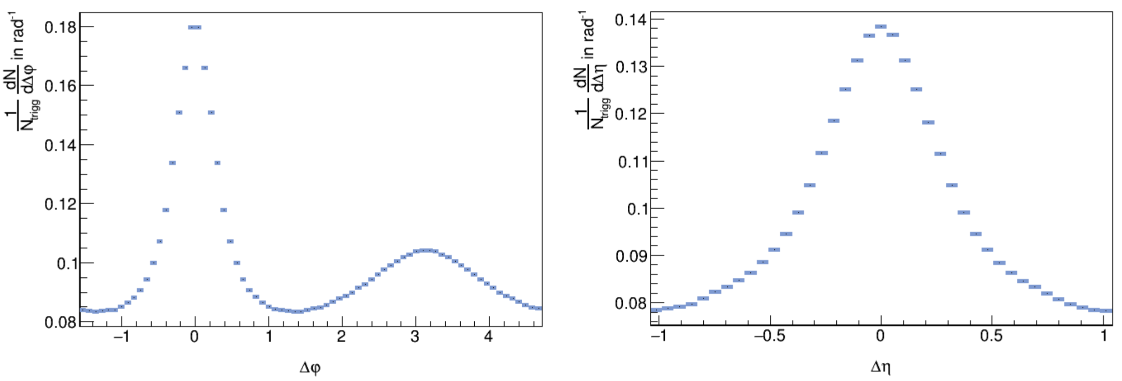

(a) $\Delta\varphi$ projection

(b) $\Delta\eta$ projection

Figure 4.3: Shown are the projections of the h-h correlation function at 3-4 GeV/c. At the $\Delta\varphi$ projection both the away-side at $\Delta\varphi = \pi$ and near-side peak at $\Delta\varphi = 0$ are visible.

4.4.1 Single Gauss fit

At first, to get a brief overview on the FWHMs a single Gauss fit was used to describe the peaks in both projections. The preinstalled Gaussian function 'gauss' only has three parameters, so the curve can not be shifted vertically. In our case this is problematic, because as one can see in Figure 4.3a and Figure 4.3b, the measured points do not start at zero. Still, this function is of good use to find starting parameters for a Gaussian function which is movable vertically. We can define this as [27]:

$$g = \frac{1}{\sqrt{2\pi\sigma^2}} \cdot \exp\left(-\frac{1}{2}\left(\frac{x-\mu}{\sigma}\right)^2\right) + y \equiv ps_0 \cdot \exp\left(-\frac{1}{2}\left(\frac{x-ps_1}{ps_2}\right)^2\right) + ps_3. \tag{4.4.1}$$

The amplitude $\frac{1}{\sqrt{2\pi\sigma^2}}$ corresponds in our function to parameter ps_0, the mean value μ to ps_1, the standard deviation σ to ps_2 and the vertical shift y to ps_3.

4.4.2 Double Gauss fit

The single Gauss function describes the data just roughly. To determine the FWHM of the near-side and away-side peak of the $\Delta\varphi$ projection or the peak in the $\Delta\eta$ projection more accurate, we used a double Gaussian function existing out of the sum of two Gaussian functions, whereas one describes the top part of the peak while the other describes better the width of the bottom part of the peak. This procedure is for every peak and projection basically the same. At first, we therefore fit the implemented Gauss function for just the top part of the peak and another one for the whole peak, as seen exemplary in Figure 4.4. The two fits do not describe the data very well. The parameters of the implemented Gauss

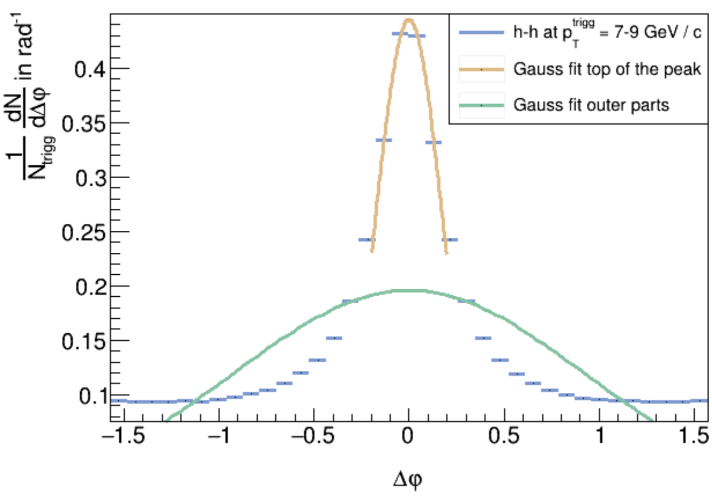

Figure 4.4: Two single not shifted Gaussian fits are plotted exemplary for the near-side projection of h-h correlation at $p_T^{\mathrm{trigg}} = 7\text{-}9\,\mathrm{GeV/c}$ whereas the yellow one describes better the peak of the curve and the green one the outer parts.

functions get, also everywhere else saved and then used as the start values of the shifted Gauss function. For the fourth parameter, the minimum of data points was determined and used as start value. By comparing Figure 4.4 and Figure 4.5, one can see that the two shifted Gauss functions describe the data sets already much better than the not shifted Gauss functions. To combine both of the shifted Gauss functions, the double Gauss function

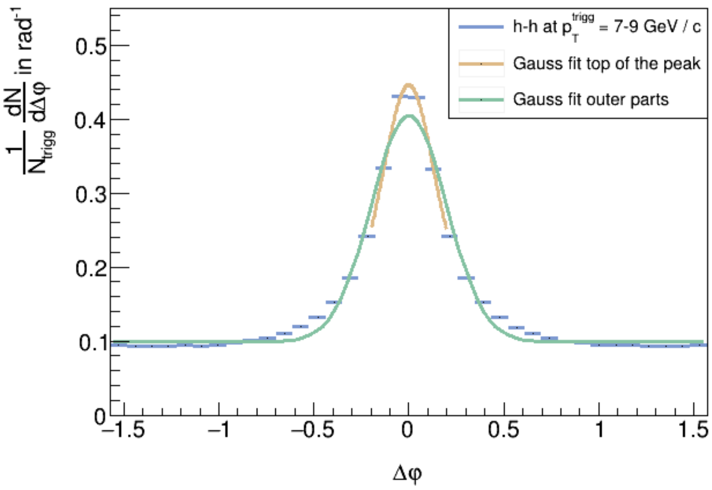

Figure 4.5: Two single shifted Gaussian fits are displayed over the same data as Figure 4.4 whereas the yellow one describes better the peak of the curve and the green one the outer parts.

gets defined as:

$$G = p_0 \cdot \exp\left(-\frac{1}{2}\left(\frac{x-p_1}{p_2}\right)^2\right) + p_3 \cdot \exp\left(-\frac{1}{2}\left(\frac{x-p_4}{p_5}\right)^2\right) + p_6 \tag{4.4.2}$$

For the double Gauss fit, the parameters of the shifted Gauss functions are used as start values. If the double Gauss fit do not describe the data well, one had to look at anomalies of the single parameters. Subsequently, extra constrains of the range had to be made.

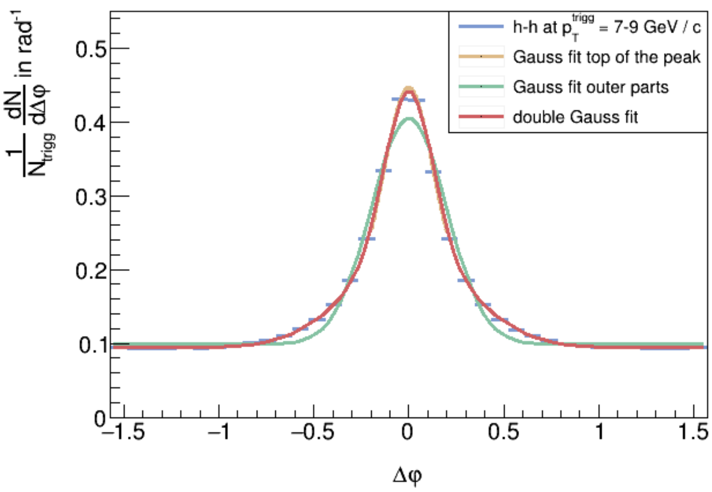

Figure 4.6: The double Gauss fit colored red resulting from the two single Gauss fits which are yellow and green which were already displayed in Figure 4.5.

4.4.3 Uncertainties

The uncertainties of the double Gaussian function got calculated via the Gaussian error propagation. To be precise the uncertainties are computed as:

$$u(G) = \sqrt{\left(\frac{\partial G}{\partial p_0}u(p_0)\right)^2 + \left(\frac{\partial G}{\partial p_2}u(p_1)\right)^2 + ... + \left(\frac{\partial G}{\partial p_6}u(p_6)\right)^2}. \tag{4.4.3}$$

$G(p_0, p_1, ...p_6)$ is the function with the accordingly parameters $p_0, p_1, ...p_6$ which have an uncertainty of $u(p_0), ..., u(p_6)$. The parameter's uncertainties got taken from the fit with the command "GetParError".

4.5 Full width at half maximum

4.5.1 Single Gauss fit

The FWHM of the single Gauss fit can be easily calculated via the standard deviation of the fit ps_2 with:

$$\text{FWHM} = 2 \cdot \sqrt{2 \cdot \ln(2)} \cdot ps_2. \tag{4.5.1}$$

4.5.2 Double Gauss fit

The first step to measure the half-width of the double Gauss fit is to determine the minimum and maximum. For that, the function gets sampled with an increment of 0.001. By using two if-loops, one for the minimum and one for the maximum, those values can get determinated via comparing the current value with the current maximum or minimum. We then define the half value as:

$$\text{half value} = \frac{\text{min} + \text{max}}{2}. \tag{4.5.2}$$

The function gets again sampled with the same increment, by first investigating into the left side of the fit and then the right side to find both $\Delta\varphi_{\text{left}}$ and $\Delta\varphi_{\text{right}}$ results at the half-value. The difference of these values is defined as the full width at half maximum (FWHM).

4.5.3 Uncertainties

The uncertainty of the FWHM of the single Gauss fit gets calculated via Gaussian error propagation resulting in:

$$u(\text{FWHM}) = 2 \cdot \sqrt{2 \cdot \ln(2)} \cdot u(ps_2). \tag{4.5.3}$$

The uncertainty of the standard deviation $u(ps_2)$ got taken from the fit with the command "GetParError".
The uncertainty of the FWHM of the double Gauss fits is based on the uncertainties of the half-widths. The uncertainties of the half-widths $u(\Delta\varphi_{\text{left}})$ and $u(\Delta\varphi_{\text{right}})$ are calculated as

described in section 4.4.3. Because the FWHM is the difference between the half-widths, the uncertainty of the FWHMs is based on the Gaussian error propagation:

$$u(\mathrm{FWHM}) = \sqrt{u^2(\Delta\varphi_{\mathrm{left}}) + u^2(\Delta\varphi_{\mathrm{right}})}. \tag{4.5.4}$$

The errorbars towards the x-axis display the $p_{\mathrm{T}}^{\mathrm{trigg}}$-intervals of the data.

4.6 Results and discussion

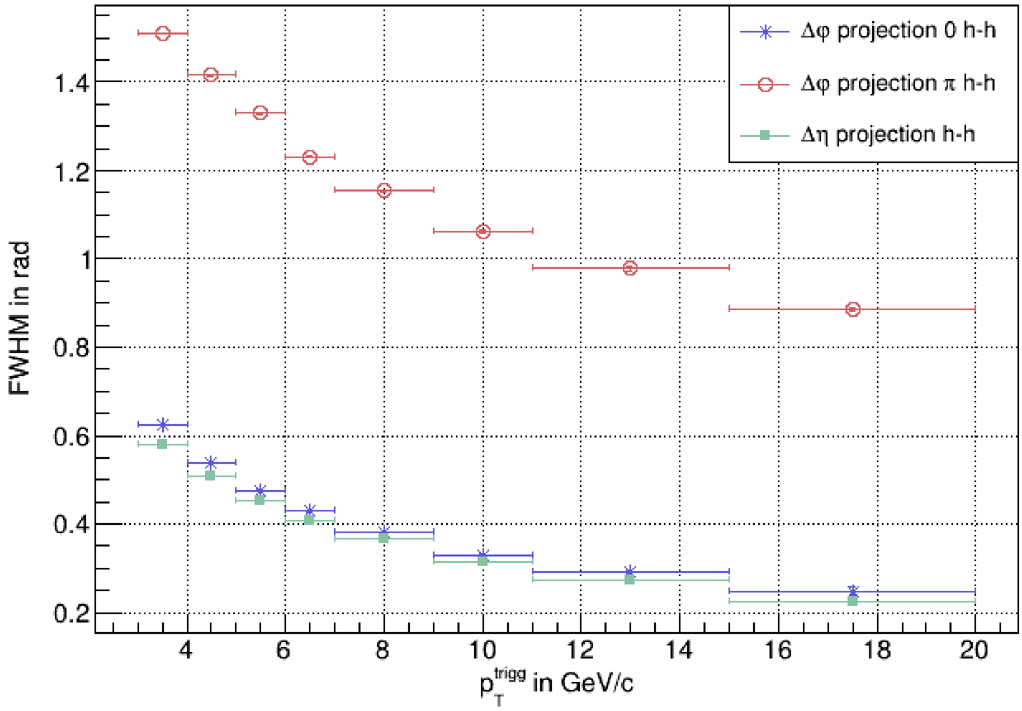

Figure 4.7: Plotted are the resulting FWHMs of the double Gauss fits of the h-h correlation projection against their transverse momentum.

Figure 4.7 shows the FWHMs of the projections of the h-h correlation plotted against the $p_{\mathrm{T}}^{\mathrm{trigg}}$ of the trigger particle. The figure displays that the away-side peak is round about two times wider than the near side-peak. There is an decrease of the FWHM with higher $p_{\mathrm{T}}^{\mathrm{trigg}}$ discernible. The FWHMs of the $\Delta\varphi$ projection of the near-side peak appear wider than the FWHMs of the $\Delta\eta$ projection.

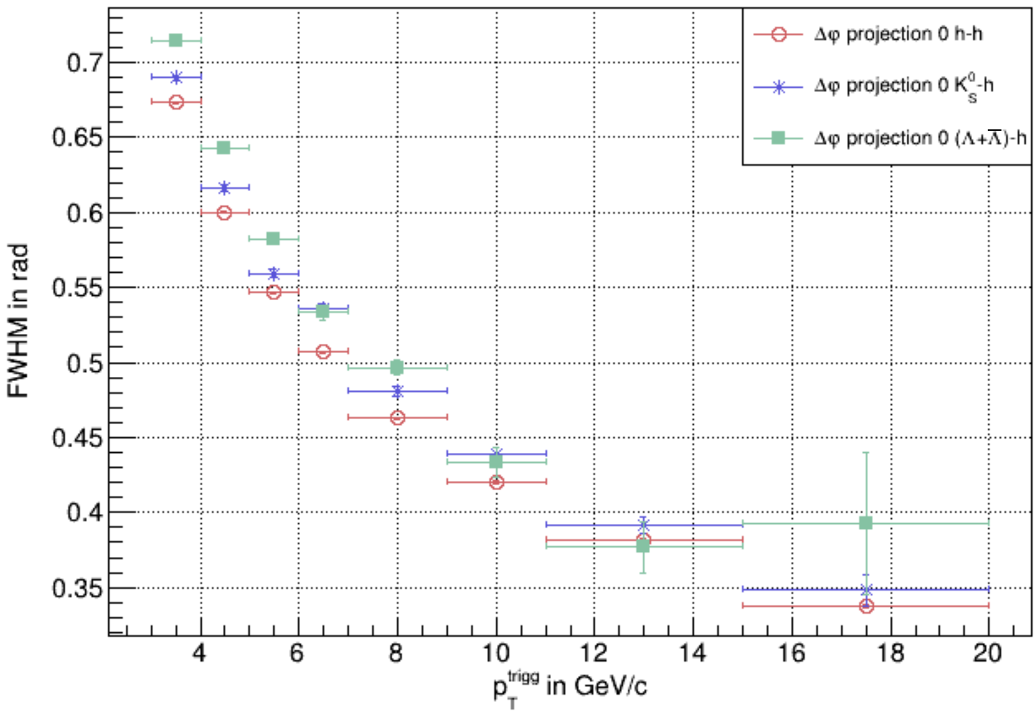

Figure 4.8: Displayed are the resulting FWHMs of the single Gauss fits of the near-side peak of the $\Delta\varphi$ projection against their transverse momentum.

The resulting FWHMs of the single Gaussian fits of the near-side peaks of the $\Delta\varphi$ projection are displayed in Figure 4.8. For the $p_{\mathrm{T}}^{\mathrm{trigg}}$-interval of 3-9 GeV/c the $(\Lambda + \overline{\Lambda})$-h correlation functions have the highest FWHM, except for the interval of $p_{\mathrm{T}}^{\mathrm{trigg}}$ =6-7 GeV/c where the FWHM of $\mathrm{K}^0_{\mathrm{S}}$-h is round about as high as the $(\Lambda + \overline{\Lambda})$-h. The h-h projection has nearly always the lowest FWHM compared to the other correlation functions, just in the interval of $p_{\mathrm{T}}^{\mathrm{trigg}}$ =11-15 GeV/c the $(\Lambda + \overline{\Lambda})$-h function has the lowest FWHM but it is still compatible within the uncertainty.

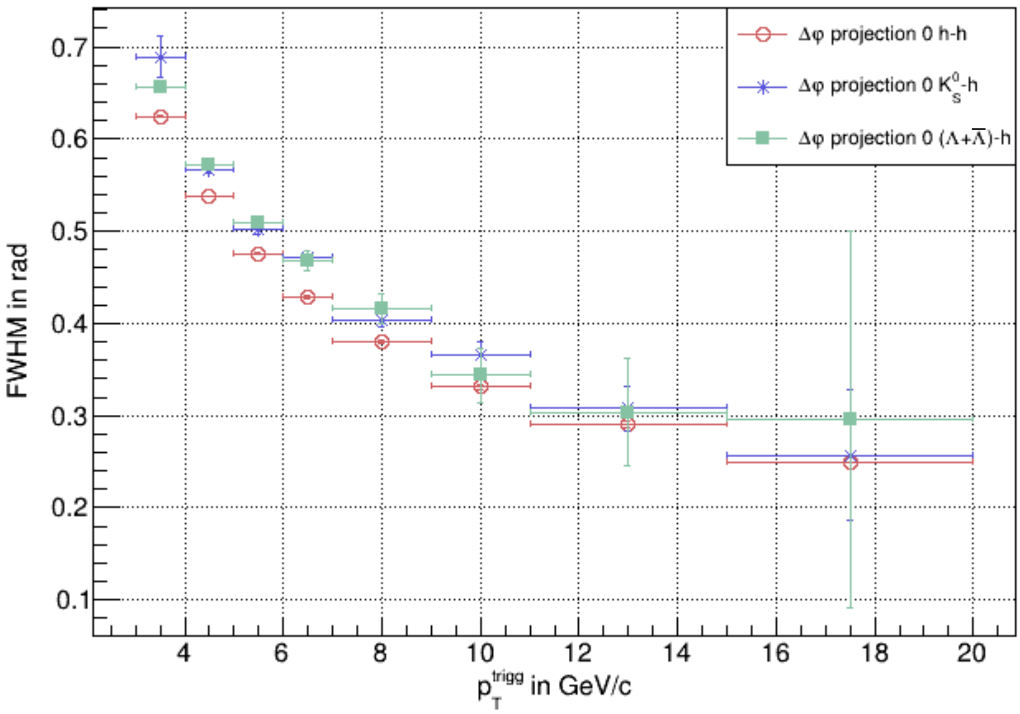

Figure 4.9: Displayed are the resulting FWHMs of the double Gauss fits of the nearside peak of the $\Delta\varphi$ projection against their transverse momentum.

In Figure 4.9, there are displayed the FWHMs of the peak around $\Delta\varphi = 0$ of the $\Delta\varphi$ projection. The h-h correlation seems to have the smallest FWHMs whilst sometimes the $(\Lambda + \overline{\Lambda})$-h correlation and sometimes the $\mathrm{K_S^0}$-h correlation function have the largest FWHM which are mostly compatible within uncertainties. The general trend of decreasing FWHM with rising p_T is given by all three correlation functions.

By comparing the single Gauss with the double Gauss fits, one especially notices the larger uncertainties of the FWHMs of the double gauss fit, in particular for $p_\mathrm{T}^\mathrm{trigg} < 11\,\mathrm{GeV/c}$. While, the largest FWHM is estimated for the $(\Lambda + \overline{\Lambda})$-h peak with the single Gauss method in the lowest $p_\mathrm{T}^\mathrm{trigg}$ bin, with the double gauss fit, the $\mathrm{K_S^0}$-h peak is estimated as the widest one. The FWHMs of the single Gaussian fit are in general around 0.05 rad broader than those of the double Gauss fit.

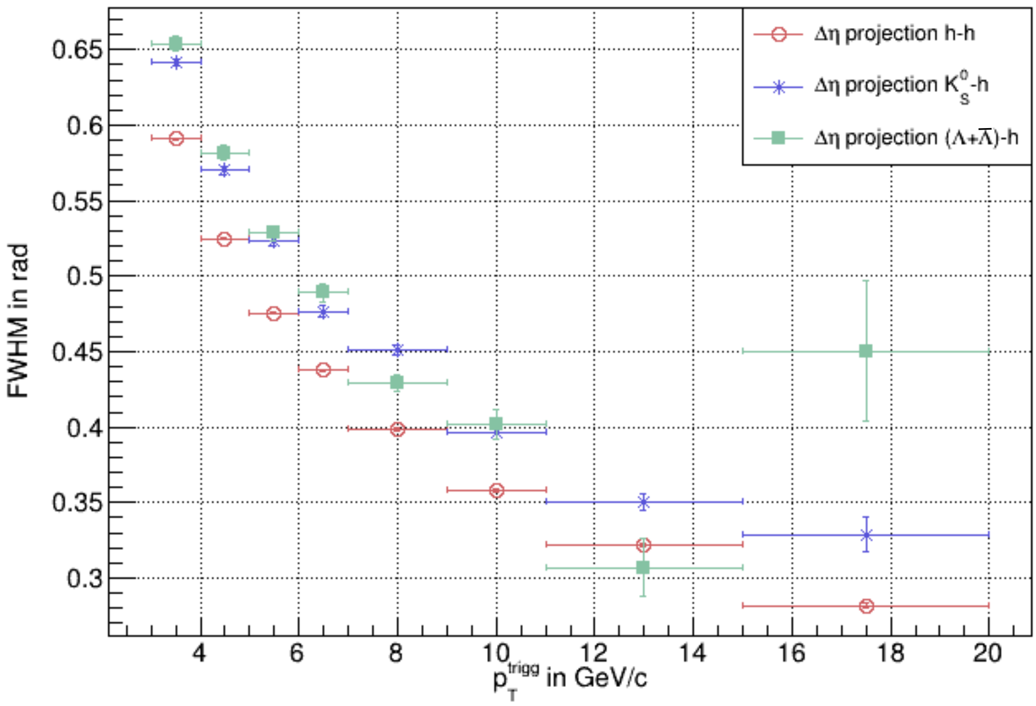

Figure 4.10: Displayed are the resulting FWHMs of the single Gauss fits of the $\Delta\eta$ projection peak against their transverse momentum.

In Figure 4.10 the resulting FWHMs of the single Gauss fits of the $\Delta\eta$ projection are shown. Mostly, the FWHMs of the h-h correlations are the smallest. Except for $p_{\mathrm{T}}^{\mathrm{trigg}}$ =11-15 GeV/c where the $(\Lambda + \overline{\Lambda})$-h correlation has the narrowest FWHM. On the other hand, the FWHMs of the $(\Lambda + \overline{\Lambda})$-h at $p_{\mathrm{T}}^{\mathrm{trigg}} < 7\,\mathrm{GeV/c}$ are always higher than of the h-h and $\mathrm{K^0_S}$-h correlation. A general decreasing trend of the FWHM with larger transverse momentum is given by all three correlations but especially for $\mathrm{K^0_S}$-h and h-h.

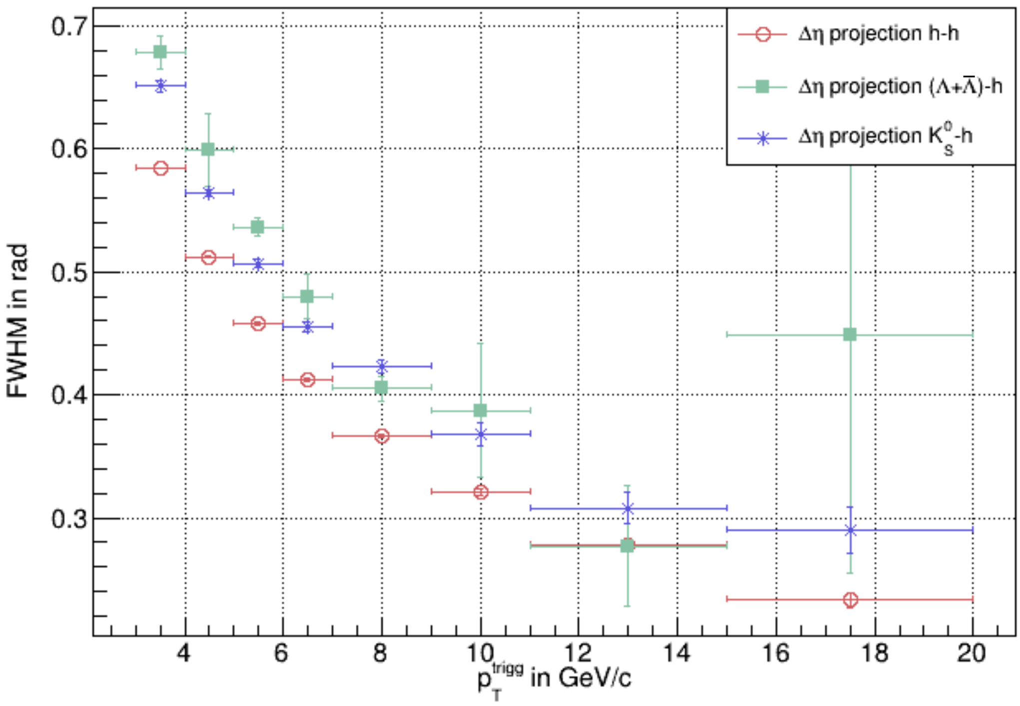

Figure 4.11: Shown are the resulting FWHMs of the double Gauss fits of the $\Delta\eta$ projection.

In Figure 4.11 the FWHM of the $\Delta\eta$ peak are shown. The h-h correlation seems to have the smallest FWHM at every $p_{\mathrm{T}}^{\mathrm{trigg}}$-range except for 11-15 GeV/c, where the $(\Lambda + \overline{\Lambda})$-h correlation has around the same FWHM, but it is still compatible within uncertainty. In contrast, the $(\Lambda + \overline{\Lambda})$-h correlation has the widest peak for most of the $p_{\mathrm{T}}^{\mathrm{trigg}}$-intervals especially for $p_{\mathrm{T}}^{\mathrm{trigg}}$-ranges lower than 7 GeV/c. The FWHM of the $\mathrm{K}_{\mathrm{S}}^{0}$-h correlation shows a consistently decreasing trend for the FWHM with higher $p_{\mathrm{T}}^{\mathrm{trigg}}$ as well as the h-h correlation.

The single Gauss fit and the double Gauss fit are both showing comparatively small FWHMs at $p_{\mathrm{T}}^{\mathrm{trigg}}$ =11-15 Ge/V for the $(\Lambda + \overline{\Lambda})$-h correlation function. Based on the large uncertainty, this is only a statistical fluctuation as the correlation function is lacking on statistics. The single Gaussian fit shows this more extreme, because there $(\Lambda + \overline{\Lambda})$-h has even a smaller FWHM as the h-h correlation function. Both plots show that for $p_{\mathrm{T}}^{\mathrm{trigg}}$-ranges lower than 7 GeV/c $(\Lambda + \overline{\Lambda})$-h has the largest FWHM.

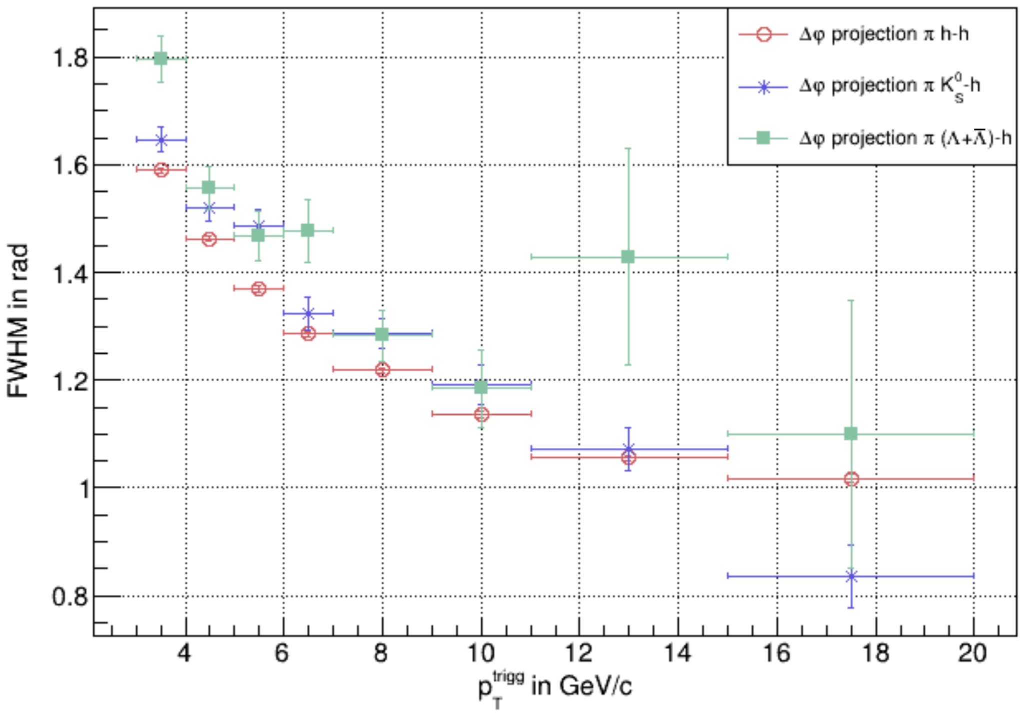

Figure 4.12: Displayed are the resulting FWHMs of the single Gauss fits of the away-side peak of the $\Delta\varphi$ projection against their transverse momentum.

Figure 4.12 displays the FWHMs of the single Gauss fit of the away-side peak. A general decreasing trend in FWHM with higher $p_{\mathrm{T}}^{\mathrm{trigg}}$ is given. The largest abberation from this is the very large FWHM of the $(\Lambda + \overline{\Lambda})$-h at a $p_{\mathrm{T}}^{\mathrm{trigg}}$ = 11-15 GeV/c which is a fluctuation caused by the small statistics. The h-h projection has always the lowest FWHM compared to the other two functions, except for $p_{\mathrm{T}}^{\mathrm{trigg}}$ =15-20 GeV/c where the $\mathrm{K}^0_{\mathrm{S}}$-h correlation is the lowest one again probably caused by the lack of statistics in this $p_{\mathrm{T}}^{\mathrm{trigg}}$ region.

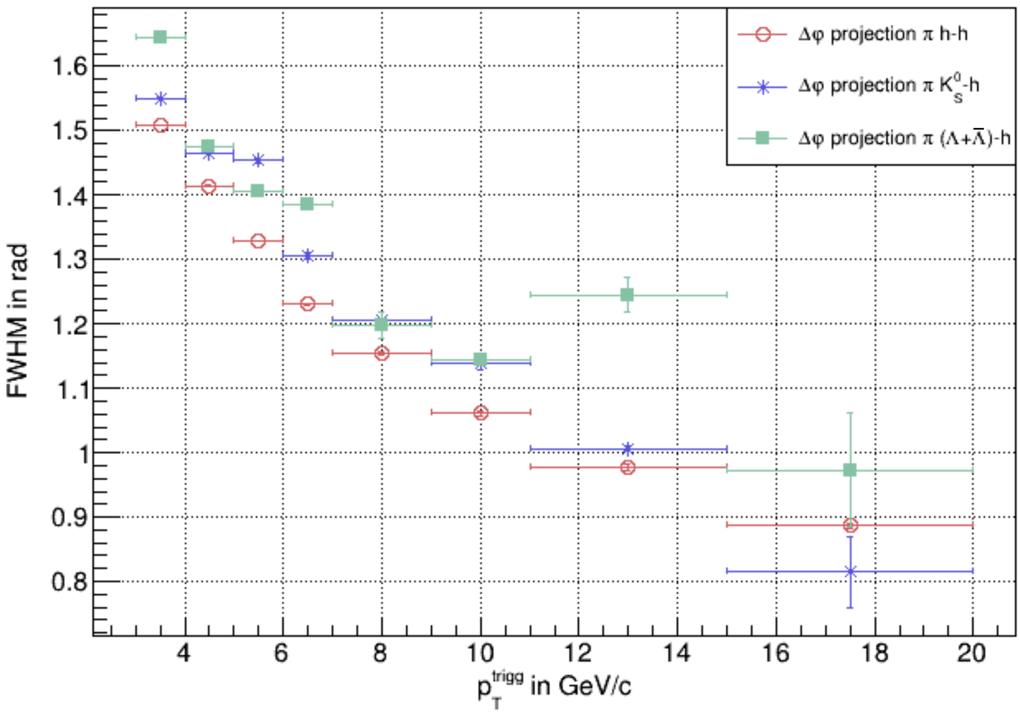

Figure 4.13: Depicted are the resulting FWHMs of the double Gauss fits of the $\Delta\varphi \approx \pi$ projection.

The general decreasing trend for the FWHM with higher $p_{\mathrm{T}}^{\mathrm{trigg}}$ is also visible in Figure 4.13. The huge FWHM at $p_{\mathrm{T}}^{\mathrm{trigg}}$-range of 11-15 GeV/c for the $(\Lambda+\overline{\Lambda})$-h correlation is the largest exemption. Another abnormality is the very low FWHM of the $\mathrm{K}^0_{\mathrm{S}}$-h correlation at 15-20 GeV/c.

The plots of the FWHM of the single and double Gaussian fits look in total very similar. The FWHMs of the single Gaussian fits have larger uncertainties and for $p_{\mathrm{T}}^{\mathrm{trigg}} < 11\mathrm{GeV/c}$ larger FWHMs.

The results show that the $(\Lambda + \overline{\Lambda})$-h correlations mostly and especially for small $p_{\mathrm{T}}^{\mathrm{trigg}}$ result in wider jets than h-h and $\mathrm{K}^0_{\mathrm{S}}$-h. With the knowledge that gluon jets have a larger width than quark-antiquark jets, $(\Lambda + \overline{\Lambda})$-h jets seem to be more gluon induced that the other ones. The FWHM of $\mathrm{K}^0_{\mathrm{S}}$-h is also higher then the of h-h. Except for the $\Delta\varphi$ projection π at 15-20 GeV/c. The uncertainty of the $(\Lambda + \overline{\Lambda})$-h FWHMs are mostly the highst because their peaks were especially for large $p_{\mathrm{T}}^{\mathrm{trigg}}$ not much well-shaped due to the lack of statistics. Another conspicuity of the $(\Lambda + \overline{\Lambda})$-h correlation is their very large or very low FWHM at 11-15 GeV/c, which could be caused by fluctuations. A total decreasing trend in FWHM with higher $p_{\mathrm{T}}^{\mathrm{trigg}}$ is given by all correlation function peaks as a consequence of the more collimated jets produced in harder processes. The differences in the resulting FWHMs of the single and double Gaussian fits show the importance of the more elaborate double Gaussian fit, which describes the data points much better.

5 Conclusion

Within this thesis about jet widths, the needed theoretical and experimental background is introduced shortly. Afterwards the actual data and its corrections are described. The correlation function as method for determining jet widths is explained. The projections $\Delta\varphi$ and $\Delta\eta$ resulted from h-h, K^0_S-h and $(\Lambda + \overline{\Lambda})$-h correlation functions are calculated with data from pp collisions with $\sqrt{s} = 13\,\text{TeV}$ at the ALICE detector. In those projections, the FWHM of the near- and away-side peak is determined via fitting single or double Gaussian fits with the program ROOT.

The data are showing that the near-side peak of the $(\Lambda + \overline{\Lambda})$-h correlation function is the widest of the studied ones. Based on the knowledge that the gluon jets are wider and produce more Λ baryons relative to charged hadrons as quark jets, one can conclude that triggering with Λ, a bias towards gluon jets is present. The strangeness of the trigger particle also seems to have a small influence on the jet width as the K^0_S-h correlation function has mostly also broader FWHMs as the h-h correlation function. Also a general decreasing trend in FWHM for larger p_T^{trigg} was shown which is a consequence of the more collimated jets produced in harder processes.

This analysis could be improved by using more statistics because especially for $(\Lambda + \overline{\Lambda})$-h correlation there are big fluctuations. The FWHM could be even more accurate by using a larger amount of Gaussian fits per peak or finding a function which describes the data points better. An improvement to investigate further in transverse momenta could be to also distinguish between different p_T^{assoc} intervals for the Gaussian fits. On the other hand, the lower amount of events per interval of momentum would lead to even larger fluctuations. Moreover, the resulting FWHMs could also get compared to simulations.

Bibliography

[1] K. Ackerstaff et al. "Production of $\mathrm{K_S^0}$ and Λ in quark and gluon jets from $\mathrm{Z^0}$ decay". In: *The European Physical Journal C* 8.2 (Apr. 1999), pp. 241–254. ISSN: 1434-6052. URL: `http://dx.doi.org/10.1007/s100529901058`.

[2] Jörn Bleck-Neuhaus. *Elementare Teilchen. Von den Atomen über das Standard-Modell bis zum Higgs-Boson.* Springer-Verlag GmbH, 2013. ISBN: 9783642325786.

[3] B. Povh, K. Rith, *et al. Particles and Nuclei. An Introduction to the Physical Concepts.* Springer-Verlag GmbH, 2015. ISBN: 9783662463208.

[4] Cush. URL: `https://upload.wikimedia.org/wikipedia/commons/a/a3/Standard_Model_of_Elementary_Particles_Anti.svg`.

[5] Particle Data Group. *The Review of Particle Physics (2021).* Accessed: 2021-08-20. 2021. URL: `https://pdg.lbl.gov/`.

[6] Claude Amsler. *Kern- und Teilchenphysik.* vdf Hochschulverlag AG, 2007. ISBN: 9783825228859.

[7] ALICE Collaboration. *K_S^0- and (anti-)Λ-hadron correlations in pp collisions at $\sqrt{s} = 13$ TeV.* 2021. arXiv: `2107.11209 [nucl-ex]`.

[8] A. Maire. "Topological selections for V0 (K0s, Lambda) and Cascade (Xi, Omega) reconstruction in ALICE". General Photo. Nov. 2011. URL: `https://cds.cern.ch/record/2030272`.

[9] Bo Andersson. *The Lund Model.* Cambridge Monographs on Particle Physics, Nuclear Physics and Cosmology. Cambridge University Press, 1998. DOI: `10.1017/CBO9780511524363`.

[10] G. Abbiendi et al. "Experimental properties of gluon and quark jets from a point source". In: *The European Physical Journal C* 11.2 (Nov. 1999), pp. 217–238. ISSN: 1434-6052. DOI: `10.1007/s100529900181`. URL: `http://dx.doi.org/10.1007/s100529900181`.

[11] R J Akers *et al.* "A model independent measurement of quark and gluon jet properties and differences". In: *Z. Phys. C* 68 (May 1995), 179–202. 13 p. URL: `http://cds.cern.ch/record/283142`.

[12] Christian Klein-Bösing. *private conversation.*

[13] Matthew D. Schwartz. *TASI Lectures on Collider Physics.* 2017. arXiv: `1709.04533 [hep-ph]`.

[14] C.Y. Wong. *Introduction to High-energy Heavy-ion Collisions*. Introduction to High-energy Heavy-ion Collisions. World Scientific, 1994. ISBN: 9789810202637. URL: https://books.google.de/books?id=Fnxvrdj2NOQC.

[15] *ALICE*. https://alice.cern/. Accessed: 2021-08-24.

[16] Lyndon Evans and Philip Bryant. "LHC Machine". In: *Journal of Instrumentation* 3.08 (Aug. 2008), S08001–S08001. DOI: 10.1088/1748-0221/3/08/s08001. URL: https://doi.org/10.1088/1748-0221/3/08/s08001.

[17] *CERN COURIER*. https://cerncourier.com/a/the-super-lhc-is-on-the-starting-blocks/. Accessed: 2021-08-25.

[18] *CERN*. https://home.cern/resources/faqs?text=&field_p_faq_display_topic_target_id=1114&field_p_faq_display_audience_target_id=All. Accessed: 2021-08-25.

[19] Brüning. "LHC Design Report". In: CERN Yellow Reports: Monographs (2004). DOI: 10.5170/CERN-2004-003-V-1. URL: https://cds.cern.ch/record/782076.

[20] "Performance of the ALICE experiment at the CERN LHC". In: *International Journal of Modern Physics A* 29.24 (Sept. 2014), p. 1430044. ISSN: 1793-656X. DOI: 10.1142/s0217751x14300440. URL: http://dx.doi.org/10.1142/S0217751X14300440.

[21] Francesco Noferini and. "ALICE results from Run-1 and Run-2 and perspectives for Run-3 and Run-4". In: *Journal of Physics: Conference Series* 1014 (May 2018), p. 012010. DOI: 10.1088/1742-6596/1014/1/012010. URL: https://doi.org/10.1088/1742-6596/1014/1/012010.

[22] Lucia Anna Tarasovicova. *Identified particle correlations at high pT, 2021*. ALICE internal note https://alice-notes.web.cern.ch/node/902. Accessed: 2021-09-02.

[23] Zachary Marshal. *Simulation of Pile-up in the ATLAS Experiment*. https://cds.cern.ch/record/1616394/files/ATL-SOFT-PROC-2013-030.pdf. Accessed: 2021-11-04.

[24] S. Chatrchyan *et al.* "Long-range and short-range dihadron angular correlations in central PbPb collisions at $\sqrt{s_{\mathrm{NN}}}$ =2.76 TeV". In: *Journal of High Energy Physics* 2011.7 (July 2011). ISSN: 1029-8479. DOI: 10.1007/jhep07(2011)076. URL: http://dx.doi.org/10.1007/JHEP07(2011)076.

[25] Rene Brun and Fons Rademakers. "ROOT An object oriented data analysis framework". In: *Nuclear Instruments and Methods in Physics Research Section A: Accelerators, Spectrometers, Detectors and Associated Equipment* 389.1 (1997). New Computing Techniques in Physics Research V, pp. 81–86. ISSN: 0168-9002. DOI: https://doi.org/10.1016/S0168-9002(97)00048-X. URL: https://www.sciencedirect.com/science/article/pii/S016890029700048X.

[26] *ROOT Data Analysis Framework*. https://root.cern/. Accessed: 2021-09-30.

[27] Bronstein, Semendjajew, *et al. Taschenbuch der Mathematik*. Europa-Lehrmittel, 2016. ISBN: 9783808557907.